frontiers | Frontiers in Physics

TYPE Original Research
PUBLISHED 09 August 2022
DOI 10.3389/fphy.2022.862156

OPEN ACCESS

EDITED BY
Ivan Marri,
University of Modena and Reggio Emilia, Italy

REVIEWED BY
Dong Mao,
Northwestern Polytechnical University, China
Cuicui Lu,
Beijing Institute of Technology, China

*CORRESPONDENCE
Hua Jie Hu,
9906242@haust.edu.cn
Xin Zhong Li,
xzli@haust.edu.cn

SPECIALTY SECTION
This article was submitted to Optics and Photonics, a section of the journal Frontiers in Physics

RECEIVED 25 January 2022
ACCEPTED 04 July 2022
PUBLISHED 09 August 2022

CITATION
Ji YW, Ma XK, Hu HJ and Li XZ (2022), Enhanced edge detection based on spin hall effect in the uniaxial crystal. *Front. Phys.* 10:862156. doi: 10.3389/fphy.2022.862156

Enhanced edge detection based on spin hall effect in the uniaxial crystal

Yan Wei Ji[1], Xi Kui Ma[1], Hua Jie Hu[2]* and Xin Zhong Li[2]*

[1]State Key Laboratory of Electrical Insulation and Power Equipment, School of Electrical Engineering, Xi'an Jiaotong University, Xi'an, SN, China, [2]School of Physics and Engineering, Henan University of Science and Technology, Luoyang, China

Optical analog computing and spatial differentiation have received great attention in many fields. In the field of biology and medicine, it is important to get the high contrast of phase images on a subwavelength scale. Compared with other methods, the optical methods based on the photonic spin Hall effect (PSHE) have the advantages of low costs and detailed detections, but this method also has the disadvantages of lower contrasts. Our work is aimed to improve the contrasts for the edges. In the study, we explore the spin Hall effect of light (SHEL) based on uniaxial crystals and investigate the effects of these crystals on spatial differentiation. It can be seen that in the elliptic–hyperbolic crystal, the PSHE can be enhanced significantly and the spatial differentiation contrasts are consistent with the enhancement of PSHE, which implies that this kind of medium would provide more possibilities in micro imaging.

KEYWORDS

photonic spin Hall effect, uniaxial crystal, edge detection, metamaterials, spin–orbit interaction

Introduction

Nowadays, information technology has changed people's daily life, and people create more and more calculation methods to improve the life quality. Optical analog computing is a widely used method to analyze the field distribution through an optical system, which has the advantages of real-time imaging, energy conservation, and simple principle [1–8]. Therefore, it is widely applied in spatial differentiation. Spatial differentiation is an important way to get information by extracting the edges from the figure, which can save the amount of information preservation and make the images clear for observation, especially in the biological and medical fields. For example, doctors can diagnose the physical condition of patients by observing the outline of red blood cells, and biologists can also use the method to explore the characteristics of plant cells [9].

There are many research studies on spatial differentiation at the subwavelength scale. Edge detections could be realized by optical systems [10, 11], such as metasurfaces [12], excited surface plasmon polaritons (SPPs) [13], or the optical bulky systems of Fourier lenses and filters [14, 15]. Methods based on SPPs or optical metasurfaces have the disadvantages of high price [16], and the preparations before

the experiments are very complex [17]. In addition, the minimum width of slots that can be distinguished based on SPPs is 2.4 μm [13], while the detection precision based on SHEL is 1.6 μm [18]. In this case, spatial differentiation methods based on PSHE have the potential for wide application for the advantages of detailed detections and low costs.

PSHE or the SHEL is a phenomenon that photons with opposite spins would drift in opposite directions perpendicular to the refractive index gradient [19–21]. The reason for the phenomenon is that when photons encounter media with the refractive index gradient during the process of transmission, the orbital angular momentum would interact with spin angular momentum, and then the photons with opposite spins would split. In other words, the reason for the PSHE is spin–orbit interaction (SOI). SOI has been investigated in the past decades [22–28]. The phenomena of SOI and PSHE often occur during the reflection and transmission process of light. Therefore, there are some researchers investigating the spatial differentiation based on PSHE at the air–prism interface [18, 29]. In this case, the mechanism of edge detections can be understood as deriving the complex amplitude of the incident light field. When a light beam passes through the phase object, the phase distributions for the passing light field are not equal to 0, while those of the blocked light field are 0. In this condition, there exist steps of phase distributions between the blocked light field and passing light field, and the discontinuity on phase generated the edges after the optical system.

To improve the contrasts of edges based on the PSHE method, we turn our attention to anisotropic material. In the past 20 years, the PSHE in a uniaxial crystal has been investigated with a positive index [30]. In addition, the SOI in certain uniaxial crystal [31] and so on [32–36] are also studied. There are three kinds of uniaxial crystals, and two of them are metamaterials with negative index. In this study, first we analyzed the PSHE in the simulation of the reflected field where a Gaussian beam is incident at the air–prism interface. By changing the index systems of uniaxial crystals, the enhancement order of PSHE among crystals with different dispersion relations is achieved more convincingly. Then, we used the optical system for spatial differentiation. In the same index system, the derivation results for different materials show that the edge contrasts C is proportional to the spin splitting distance δ of PSHE. In other words, the spatial differentiation effect is strongly consistent with the PSHE enhancement in the same index system. The simulation results also show that edge detections based on elliptic–hyperbolic crystals have significantly higher contrasts than those based on the traditional prism. These crystals are kinds of metamaterial with a negative index, which indicates the opportunities for metamaterials in micro imaging.

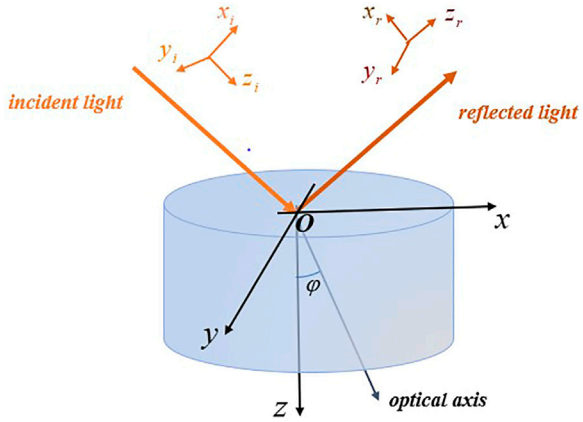

FIGURE 1
Schematic model of a uniaxial crystal sample.

Theoretical analysis

The properties of the uniaxial crystal

The reflection schematic diagram of the Gaussian beam at the air–uniaxial crystal interface is shown in Figure 1. The optical axis of the uniaxial crystal lies in the $x-z$ plane, and φ is the angle between the optical axis and the z axis.

In the study, the optical axis is set parallel to the z-axis for simplicity. According to the previous research about the beam propagating in uniaxial crystals [37–39], the constitutive relations in the anisotropic medium are given as:

$$\begin{pmatrix} D_x \\ D_y \\ D_z \end{pmatrix} = \begin{pmatrix} \varepsilon_x & 0 & 0 \\ 0 & \varepsilon_y & 0 \\ 0 & 0 & \varepsilon_z \end{pmatrix} \begin{pmatrix} E_x \\ E_y \\ E_z \end{pmatrix} \tag{1}$$

$$\begin{pmatrix} B_x \\ B_y \\ B_z \end{pmatrix} = \begin{pmatrix} \mu_x & 0 & 0 \\ 0 & \mu_y & 0 \\ 0 & 0 & \mu_z \end{pmatrix} \begin{pmatrix} H_x \\ H_y \\ H_z \end{pmatrix} \tag{2}$$

In uniaxial crystals, $\varepsilon_x = \varepsilon_y \neq \varepsilon_z, \mu_x = \mu_y \neq \mu_z$, there are two refractive indexes called ordinary refractive index n_o and extraordinary refractive index n_e. The values ofn_o and n_e stay constant for different materials in the same index system. Thus, the absolute values of permittivity and permeability for traditional uniaxial crystals are induced as

$$|\varepsilon_x| = n_o^2 \varepsilon_0 \tag{3}$$

$$|\varepsilon_y| = n_o^2 \varepsilon_0 \tag{4}$$

$$|\varepsilon_z| = n_e^2 \varepsilon_0 \tag{5}$$

$$|\mu_x| = |\mu_y| = |\mu_z| = \mu_0 \tag{6}$$

where $\varepsilon_0$and μ_0 are the permittivity and the permeability in the vacuum, respectively. For uniaxial crystals, there are three kinds of dispersion relations that are called elliptic–elliptic dispersion,

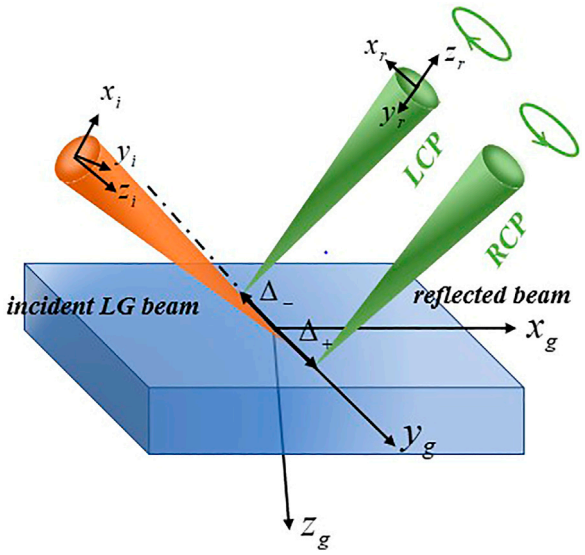

FIGURE 2
Spin splitting phenomenon schematic of Gaussian beam.

elliptic–hyperbolic dispersion, and hyperbolic–hyperbolic dispersion. The absolute values of $[\varepsilon_x, \varepsilon_y, \varepsilon_z]$ and $[\mu_x, \mu_y, \mu_z]$ are set the same among different uniaxial crystals. The direction of the z axis is marked as the principal direction. Thus, the indexes in the directions of x axis and y axis are noted with $\perp$ and z axis is noted with $\parallel$.

For elliptic–elliptic dispersion: $\varepsilon_\perp, \varepsilon_\parallel, \mu_\perp, \mu_\parallel > 0$. Materials of the other two relations are kinds of metamaterials with negative indexes. For elliptic–hyperbolic dispersion: $\varepsilon_\perp, \varepsilon_\parallel, \mu_\perp > 0$, $\mu_\parallel < 0$. For hyperbolic–hyperbolic dispersion: $\varepsilon_\perp, \mu_\parallel > 0$, $\varepsilon_\parallel, \mu_\perp < 0$. The relation curves of k_x and k_z^p, k_z^s can explain the reasons for these dispersion relation names.

The relationships of wave vectors for p wave and s wave are different and written as follows:

$$\frac{k_x^2}{\varepsilon_\parallel \mu_\perp} + \frac{k_z^{p2}}{\varepsilon_\perp \mu_\perp} = \omega^2 \tag{7}$$

$$\frac{k_x^2}{\varepsilon_\perp \mu_\parallel} + \frac{k_z^{s2}}{\varepsilon_\perp \mu_\perp} = \omega^2 \tag{8}$$

$k_x$is the incident wave vector in x-direction, $k_x = k \sin\theta$ where $k = \frac{2\pi}{\lambda}$and θ is the incident angle, k_z^p and k_z^s are the transmitted wave vector of p wave and s wave in the direction of the principal axis, respectively. Also, the r_p and r_s are Fresnel reflection coefficient for p wave and s wave in uniaxial crystals, respectively, which are given as

$$r_p = \frac{\varepsilon_\perp k_z - \varepsilon_r k_z^p}{\varepsilon_\perp k_z + \varepsilon_r k_z^p} \tag{9}$$

$$r_s = \frac{\mu_\perp k_z - \mu_r k_z^s}{\mu_\perp k_z + \mu_r k_z^s} \tag{10}$$

The ε_r and the μ_r represent the permittivity and the permeability of the air, respectively.

The photonic spin Hall effect based on uniaxial crystal

As mentioned before, the spin components of the reflected beam split owing to the SOI. In this section, the PSHE based on uniaxial crystals with different dispersion relations is explored. The spin splitting phenomenon schematic of the Gaussian beam reflection process is shown in Figure 2. The local coordinate systems attached to the incident beam and the reflected beam can be expressed as (x_i, y_i, z_i) and (x_r, y_r, z_r), respectively. The global coordinate system is represented as (x_g, y_g, z_g). After the reflection process, the opposite SOI would drift the photons with different spins to the opposite directions perpendicular to the incidence plane.

The Gaussian beam profiles can be expressed as

$$A_{in} = exp\left(-\frac{x^2 + y^2}{w_0^2}\right) exp\left(i\varphi(x, y)\right) \tag{11}$$

Here, w_0 is the beam waist of the Gaussian beams and $\varphi(x, y)$ is the phase component. In this study, it is assumed that the incident beam is horizontal polarization $\hat{e}_{ix}$. The corresponding polarization electric field can be denoted as $E_{in} = A_{in}\hat{e}_{ix}$. The angular spectrum of the reflected beam can be expressed as follows owing to the reflection matrix:

$$\tilde{E}_r = \begin{pmatrix} r_p - \frac{k_{rx}}{k} r_p' & \Delta k_{ry} \\ -\Delta k_{ry} & r_s - \frac{k_{rx}}{k} r_s' \end{pmatrix} \tilde{E}_{in} \tag{12}$$

where $\tilde{E}_{in} = \tilde{A}_{in}\hat{e}_{ix}$. The $\tilde{A}_{in}$denotes the expression of A_{in}in the form of the frequency domain. The r_p' and r_s' represent the derivative of the r_p and the r_s with respect to the incident angle θ, respectively. Also, the $\Delta = \frac{(r_p + r_s)\cot(\theta)}{k}$ in the reflection matrix. Therefore, when the incident beam has a horizontal incident polarization, the polarization state of the reflected beam is calculated as

$$\tilde{E}_r = \tilde{A}_{in}\left(r_p - \frac{k_{rx}}{k} r_p'\right)\hat{e}_{rx} - \tilde{A}_{in}\Delta k_{ry}\hat{e}_{ry} \tag{13}$$

As we know, for an arbitrarily polarized beam, its polarization state can be constructed from a vector superposition of two orthogonal circular polarizations. Usually, the left circular polarization (LCP) is noted as $\hat{e}_-$. The right circular polarization (RCP) is noted as $\hat{e}_+$. Owing to

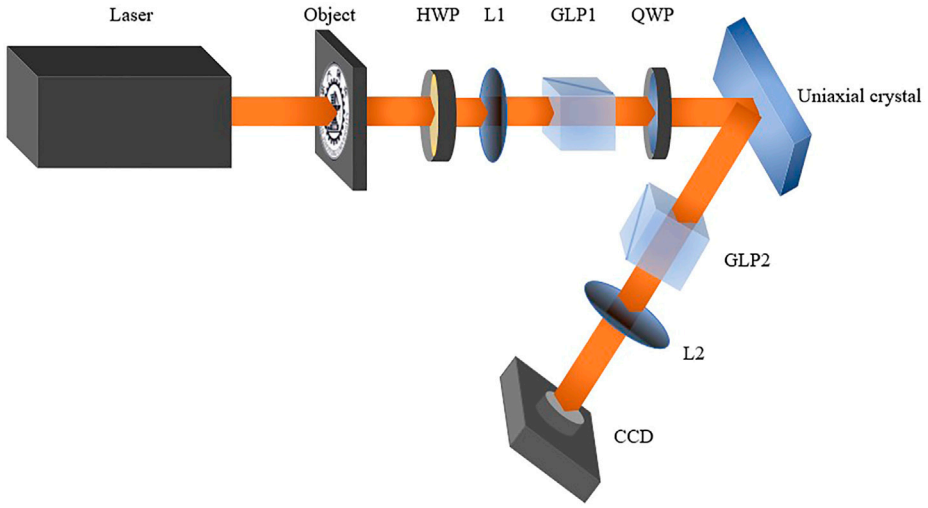

FIGURE 3
Optical setups for spatial differentiation based on PSHE.

the $\hat{e}_{\pm} = \frac{e_x \mp i e_y}{\sqrt{2}}$, the RCP and LCP components of the reflected beam can be written as

$$\tilde{E}_{r\pm} = \tilde{A}_{in}\left[\left(r_p - \frac{k_{rx}}{k} r_p^{'}\right)\hat{e}_{rx} \pm i\Delta k_{ry}\hat{e}_{ry}\right] \tag{14}$$

After the Fourier transform of $\tilde{E}_{r\pm}$, the shifts of RCP and LCP components of the reflected beam parallel to the y axis can be induced by the integral formula:

$$\delta_r^{\pm} = \frac{\iint E_{r\pm} \cdot E_r^{*} y_r dx_r dy_r}{\iint E_{r\pm} \cdot E_r^{*} dx_r dy_r} \tag{15}$$

After some straightforward calculations, the shifts for RCP and LCP components for the reflected beam can be expressed as follows [40]:

$$\delta_{\pm} = \frac{1}{kW}\left\{ \mp Re\left(r_p^{*}\Delta k\right)\right\} \tag{16}$$

Also, the W is written as

$$W = \left|r_p\right|^2 + \frac{\left(\left|r_p^{'}\right|^2 + |k\Delta|^2\right)}{k^2 w_0^2} \tag{17}$$

The spatial differentiation based on photonic spin Hall effect

There are many methods for spatial differentiation based on PSHE. It can be seen that the contrasts of the edges are relevant to the material characters of the reflecting surface. Also, the relevant optical setups [29] are shown in Figure 3.

The setup arrangement is used to detect the edges of the school badge. The half-wave plate (HWP) is used to adjust the intensity of the beam to prevent the CCD from being overexposed. The first lens (L1) is used to collimate the beam which is parallel. The first Glan laser polarizer (GLP1) and the second Glan laser polarizer (GLP2) are used to change the polarization states of the incident beam and the reflected beam. The second lens (L2) could convert the divergent beam to a parallel beam. Here, we introduce the derivation process for the spatial differentiation formula according to the relevant Ref. [29] and choose the Gaussian beam with a polarization electric field E_{in} as the incident beam. It is assumed that the polarization angle of the GLP1 is α and the beam passing through the GLP1 could be written as

$$\tilde{E}_{in} = cos\,\alpha\tilde{A}_{in}\hat{e}_{ix} + sin\,\alpha\tilde{A}_{in}\hat{e}_{iy} \tag{18}$$

Also, the Quarter Wave Plate (QWP) whose optics axis was set as $0°$ is used to change the phase of the incident beam as

$$\tilde{E}_{in} = \exp\left(-\frac{\pi}{4}i\right)\cos\alpha\tilde{A}_{in}\hat{e}_{ix} + \exp\left(\frac{\pi}{4}i\right)\sin\alpha\tilde{A}_{in}\hat{e}_{iy} \tag{19}$$

When the beam reflects at the surface of the uniaxial crystal, Eq. 19 is substituted into Eq. 12. Also, the angular spectrum of the reflected beam is written as

$$\tilde{E}_r = \exp\left(-\frac{\pi}{4}i\right)\tilde{A}_{in}\begin{bmatrix}\left(r_p - \frac{k_{rx}}{k}r_p^{'}\right)\cos\alpha + i\Delta k_{ry}\sin\alpha \\ i\left(r_s - \frac{k_{rx}}{k}r_s^{'}\right)\sin\alpha - \Delta k_{ry}\cos\alpha\end{bmatrix} \tag{20}$$

The 2×1 matrix in Eq. 20 is based on the vector units of $\hat{e}_{rx}$ and $\hat{e}_{ry}$. The polarization angle of GLP2 is set as 0°and the output electric field can be shown as

$$\tilde{E}_{rx} = \exp\left(-\frac{\pi}{4}i\right)\tilde{A}_{in}\left[\left(r_p - \frac{k_{rx}}{k}r_p^{'}\right)\cos\alpha + i\Delta k_{ry}\sin\alpha\right]\hat{e}_{rx} \tag{21}$$

In Eq. 21 above, the $\Delta_x = |\frac{r_p^{'}\cos\alpha}{k}|$ and the $\Delta_y = |\Delta\sin\alpha|$. The beam is incident at the Brewster angle in our simulations; therefore, the $r_p = 0$. In this condition, the polarization angle α is changed to the degree when the $tan\,\alpha = |\frac{r_p^{'}}{k\Delta}|$. Then, the $\Delta_x = \Delta_y$. Thus, the angular spectrum of the reflected polarized electric field can be noted as

$$\tilde{E}_{rx} \propto \left(k_x + ik_y\right)\tilde{A}_{in} \tag{22}$$

The inverse Fourier transform is performed on both sides of Eq. 22, and the result shows that

$$E_{rx} \propto \left(\frac{\partial}{\partial x} + i\frac{\partial}{\partial y}\right)A_{in} \tag{23}$$

Thus, the setup arrangements in Figure 3 could achieve the two-dimensional edge detection of the object information.

Simulation results

When a Gaussian beam reflects at the surface of a uniaxial crystal, the photons with different spins would shift to the opposite directions as shown in Eq. 16. The beam split distance between two beams δ can be deduced as follows whose absolute value is regarded as the standard for enhancement of PSHE:

$$\delta = \delta_+ - \delta_- = \frac{-2}{W}Re\left[r_p^{*}\Delta\right] \tag{24}$$

In addition, setting the value of the index C as $C = \Delta_x = \Delta_y$:

$$C = \left|\frac{r_p^{'}\Delta}{\sqrt{k^2\Delta^2 + r_p^{'2}}}\right| \tag{25}$$

C is the coefficient about k_x and k_y. Therefore, combining Eq 22 and 25, we can see that the contrasts of the edges increase with the increase of C.

Inserting the value of W from Eq. 17 into Eq. 24, it can be calculated that $|r_p|^2 \ll \frac{(|r_p^{'}|^2+|k\Delta|^2)}{k^2w_0^2}$ when the incident angle θ is the Brewster angle. Then, the absolute value of split distance δ and the expression of C can be expressed respectively as

$$|\delta| = k_1\frac{1}{\frac{\left|r_p^{'}\right|^2}{\left|\left(r_p + r_s\right)cot\,(\theta)\right|} + \left|\left(r_p + r_s\right)cot\,(\theta)\right|} \tag{26}$$

$$C = k_2\frac{1}{\sqrt{1 + \frac{\left|r_p^{'}\right|^2}{\left(r_p + r_s\right)^2 cot\,(\theta)^2}}} \tag{27}$$

The expressions of k_1 and k_2 are noted as $k_1 = |2kw_0^2Re[r_p^{*}]|$ and $k_2 = \frac{|r_p^{'}|}{k}$,respectively. It can be seen that the values of k_1 and k_2 are strongly consistent with the distributions of the index r_p and $r_p^{'}$.

Taking the index system of the quartz crystal, for example, the distributions of the $|r_p/r_s|$ with respect to the incident angle θ for different uniaxial crystals can be shown in Figure 4:

Comparing Figure 4A with Figure 4B, we can see that the change of $\mu_{\|}$ has no influence on the value of Brewster angle. The values of the Brewster angle based on elliptic–elliptic crystal and elliptic–hyperbolic crystal are the same as 56.76°. From Figure 4C, it can be found that there is no Brewster angle for beam reflecting at the surface of the crystals with hyperbolic–hyperbolic dispersion relation, which means this kind of crystal is not suitable for spatial differentiation. The distributions of beam splitting distance δ with respect to the incident angle θ based on different index systems are shown in Figure 5. The index systems of some common uniaxial crystals are used in these simulations.

The four rows correspond to the index system of quartz crystal (SiO_2), calcite crystal ($CaO.CO_2$), magnesium fluoride crystal (MgF_2), and corundum crystal (Al_2O_3). For elliptic–elliptic crystal and elliptic–hyperbolic crystal, the δ reaches its maximum value around the Brewster angle of the material. In the same index system, the maximum value of δ in the elliptic–hyperbolic crystal is a bit higher than that in the elliptic–elliptic crystal, while the value of δ in hyperbolic–hyperbolic crystal is too small to be ignored. Therefore, the hyperbolic–hyperbolic crystal is not suitable for spatial differentiation. Our work is to explore the consistency between the splitting distance δ and the spatial differentiation effect in different uniaxial crystals. In this step, the school badge of Xi'an Jiaotong University is applied for edge detection. The original picture of the badge is shown in Figure 6.

The spatial differentiation effect based on different uniaxial crystals is shown in Figure 7. Figure 7 has eight subfigures, and the figures correspond to the materials of the first two columns in Figure 5. According to the index systems, these figures are divided into four groups: (a) and (b), (c) and (d), (e) and (f), and (g) and (h). The two figures in one group share the same index system and correspond to elliptic–elliptic crystal and elliptic–hyperbolic crystal, respectively. Take Figures 7A,B, for instance, it can be seen that Figure 7B has sharper edges than Figure 7A, while all the intensity values in Figures 7A,B are normalized values based on original intensity values. In these two original figures, we take the largest intensity value as I_{max}, and all the intensity values are normalized by I_{max}. Because the Matlab software would adjust the scope of the right column automatically which would make two normalized figures have no difference to our naked eyes, then the scope of the two right columns both be reset as $0 \sim 1$. This is the

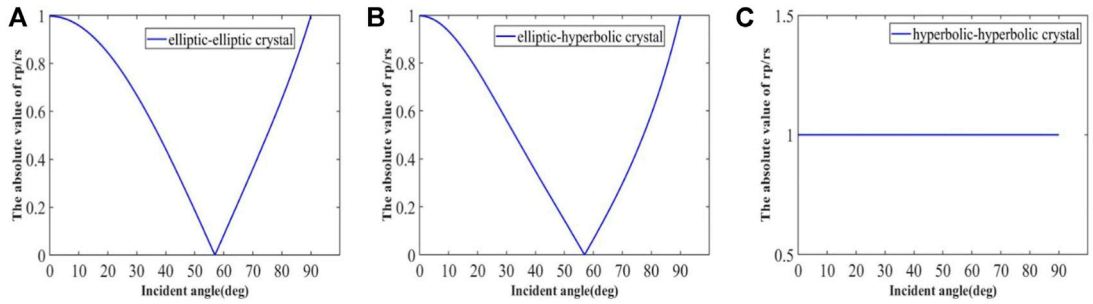

FIGURE 4
Curves of the value of $|r_p/r_s|$ with respect to **(A)**: elliptic–elliptic crystal; **(B)**: elliptic–hyperbolic crystal; **(C)**: elliptic–elliptic crystal.

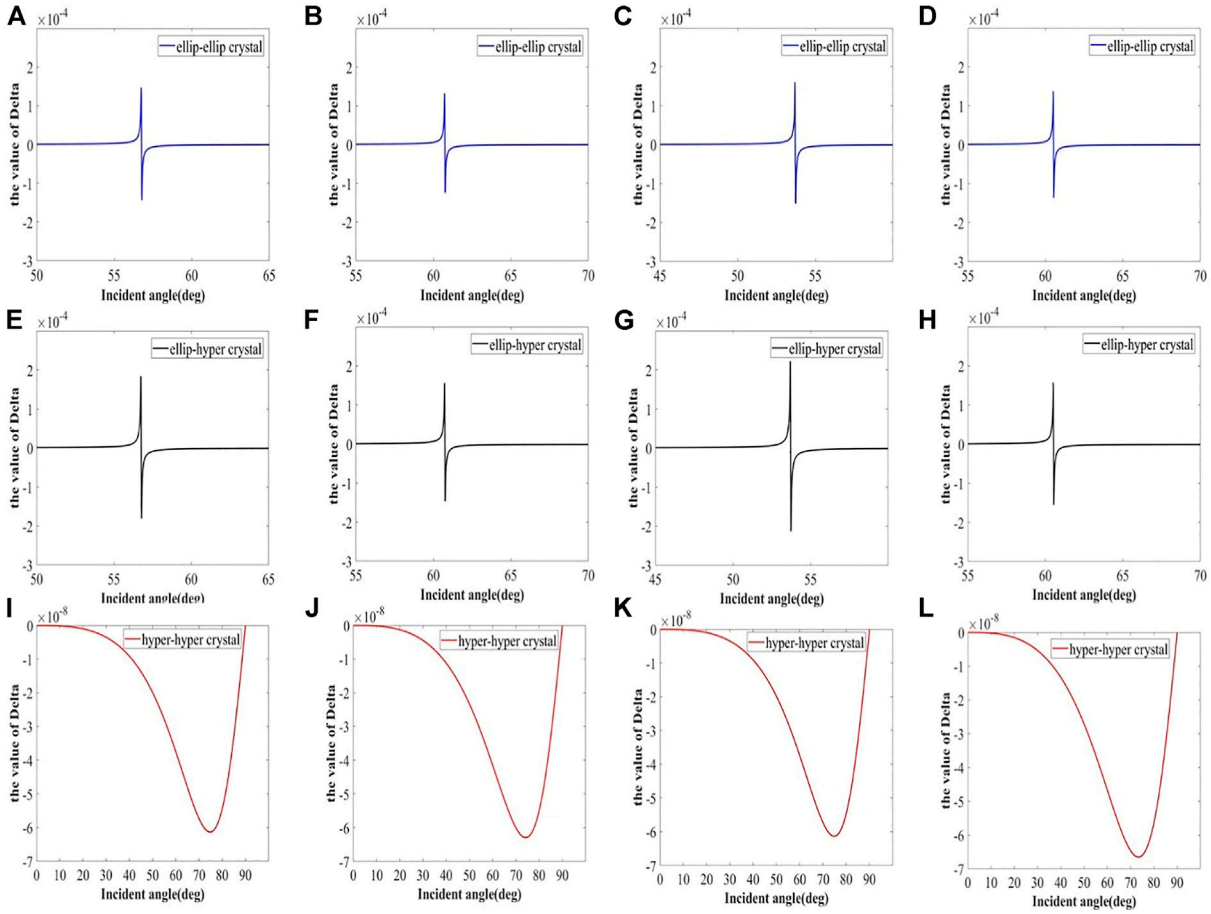

FIGURE 5
Distributions of spin splitting distance δ based on different uniaxial crystals of different index systems.

method through which we get the intensity values in Figures 7A,B, and the values of other groups are also obtained through similar operations.

It can be found that there is consistency between the maximum value of δ and the edge detection effect by comparing the subfigures in Figures 5, 7. In the same index system, the higher the maximum

FIGURE 6
Original picture of the school badge for edge detection.

value of δ, the better the spatial differentiation effect. The spatial differentiation effect is not only related to the maximum δ. For instance, the maximum value of δ in Figure 5G is much higher than that in Figure 5D, while the corresponding edge detection effect in Figure 7E is worse than that in Figure 7C. The index system also plays an important role in spatial differentiation. It is our work to accurately describe the relationship between the edge detection effect, the maximum δ, and the index system.

The index C is an important standard for measuring edge contrasts. The higher the C, the clearer the edges. Inserting Eq. 27 into Eq. 26. The $|\delta|$ can be expressed by the index C as

$$|\delta| = \frac{k_1}{k_2|r_p^{'}|} C\sqrt{1-\frac{C^2}{(k_2)^2}} \tag{28}$$

By introducing two indexes α and β, Eq. 28 can be simplified as

$$\alpha = \frac{\beta}{2} \tag{29}$$

where the $\alpha = arcsin(\frac{C}{k_2})$ and the $\beta = arcsin(\frac{2|\delta||r_p^{'}|k_2}{k_1})$. Except for the index C and $|\delta|$, Eq. 29 is strongly related to the distributions of $|r_p|$ and $|r_p^{'}|$. This relationship can explain the phenomenon we mentioned before. For instance, the elliptic–elliptic crystal and elliptic–hyperbolic crystal have the same distribution of the $|r_p|$ and $|r_p^{'}|$ in one index system, so if the $|\delta|$ is higher, the index C is higher, while in different index systems, there are different values of $r_p$and $r_P^{'}$ Therefore, the relationship between the edge detection effect and spin splitting distance is unobvious. Uniaxial crystals with negative index are kinds of metamaterials, which means they could be designed artificially. Eq. 29 gives new clues for designing crystals in edge detections.

In addition, uniaxial crystals with a certain kind of dispersion relation have great advantages over the traditional prism. The indexes of the quartz crystal are applied in these simulations, and the edge detection effects based on different materials are shown in Figure 8. There are three subfigures in Figure 8, and the

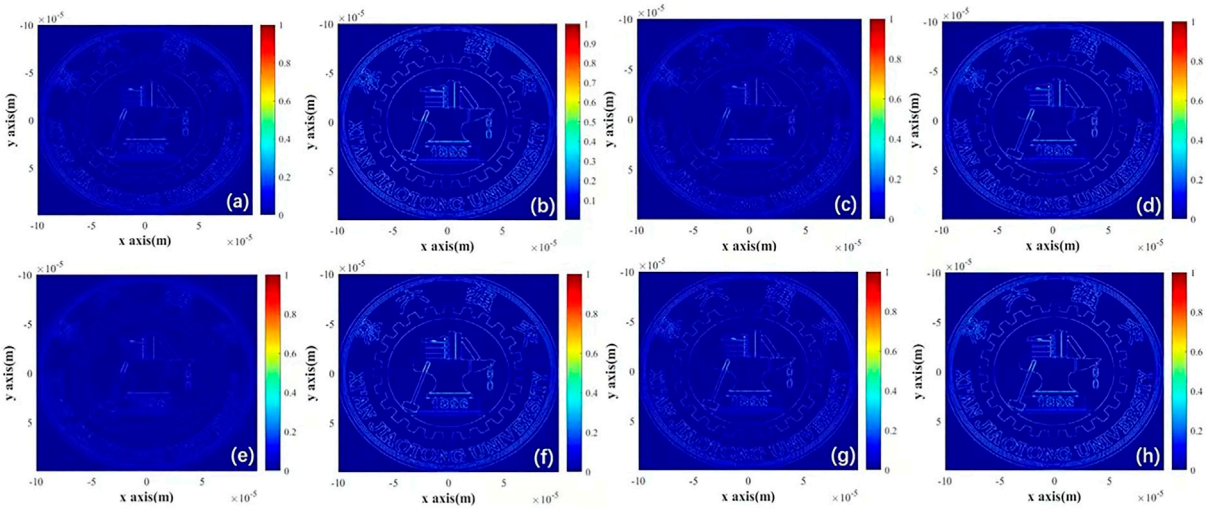

FIGURE 7
Spatial differentiation effect based on materials with different index systems.

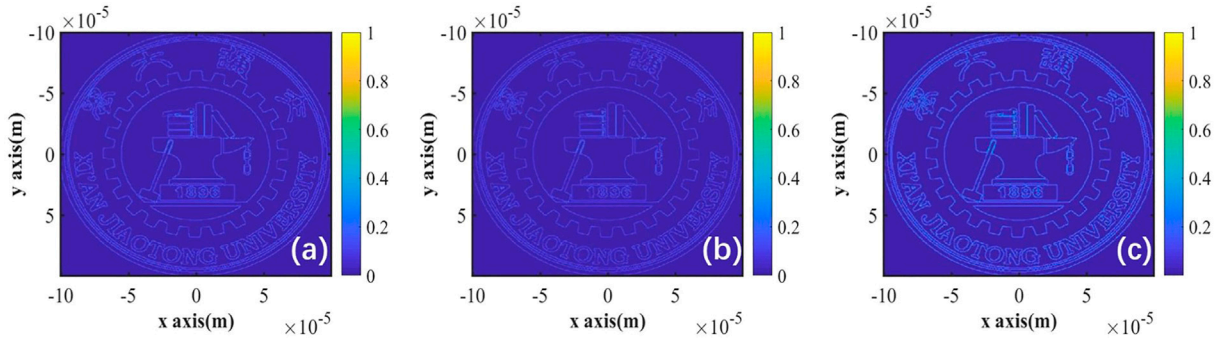

FIGURE 8
Edge detection effects based on different materials. **(A)**: traditional prism. **(B)**: elliptic–elliptic crystal. **(C)**: elliptic–hyperbolic crystal.

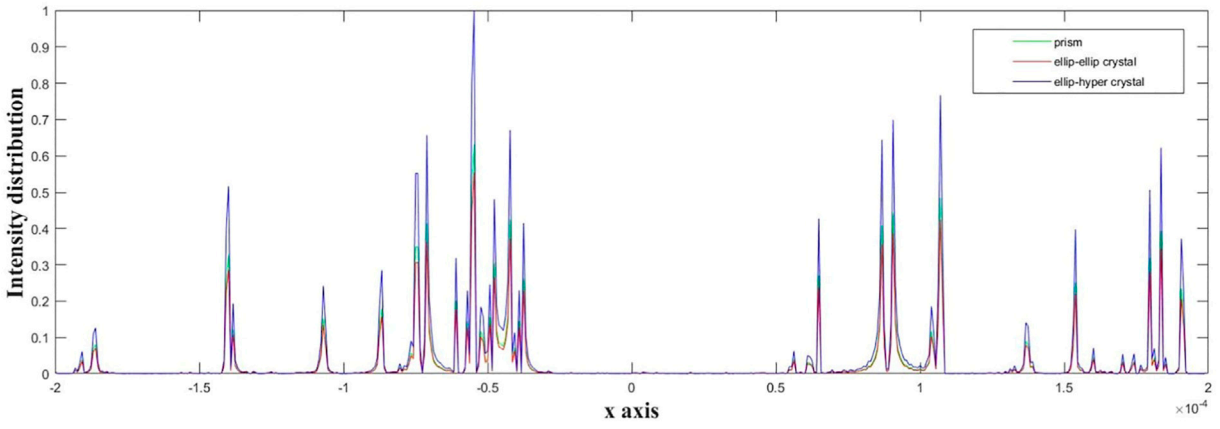

FIGURE 9
Light intensity distribution at $y = 0$ axis based on different materials.

intensity values of these subfigures are processed values based on original intensity values. The processing method is similar to that in Figure 7. We take the largest value of the three original intensity distributions as I_{max} again, and all the intensity values are normalized by I_{max}. The scope of three columns in Figure 8 are all set as $0 \sim 1$.

The effect based on the glass prism in Figure 8A is similar to that in Figure 8B based on the elliptic–elliptic crystal. The edges in both figures are not clear enough. The effect based on the elliptic–hyperbolic crystal in Figure 8C has sharper edges and conveys more figure information than the two other effects. In order to make the comparison among the three figures more intuitive, the intensity distributions based on different materials along the certain region at the axis of $y = 0$ are depicted as Figure 9. From Figure 9, it can be seen that the edge contrasts of the elliptic–hyperbolic crystal are significantly higher than those in the other two cases.

Conclusions and discussion

Our work is aimed to explore the optical characters of uniaxial crystals and compare the characters with those in the PSHE and edge detections. Setting the uniaxial crystals with different dispersion relations under the same parameter system, the numerical simulation results show the order of the PSHE enhancement as follows: elliptic–hyperbolic crystal > elliptic–elliptic crystal ≫ hyperbolic–hyperbolic crystal. For the first two materials, the value of δ would reach its maximum and minimum point when the incident angle θ distributes around the Brewster angle. The value of r_p for different θ is a constant for the last material which has no Brewster angle. Thus, the hyperbolic–hyperbolic crystal cannot be used in spatial differentiation based on PSHE. Comparing the other two uniaxial crystals, the change of parameter $\mu_\perp$ in the elliptic–hyperbolic crystal would result in the enhancement of PSHE and further improve the contrasts of edge detections. It

can be seen that the spatial differentiation effect based on the elliptic–elliptic crystal is similar to that in the traditional prism. While the effect based on the elliptic–hyperbolic crystal can reflect the edge information more clearly. Then what is the reason for the stronger enhancement of PSHE based on elliptic–hyperbolic crystal? It is known that SOI is an intrinsic reason for many physical phenomena and depends on the characters of materials. The researcher investigated that SOI based on negative index materials would show extraordinary characters [41].

Elliptic–hyperbolic uniaxial crystal is a metamaterial with a negative index, which is a kind of artificial material with special characters compared with traditional materials. The advantages of elliptic–hyperbolic material mentioned before have brought a discovery that the application of metamaterials would open up new prospects in the field of edge detection.

The applications of metamaterials are still in the stage of testing and small batch production for their high costs. However, materials used for optical differentiation usually are reused, which means that the requirements for resistance of materials are high. In the long run, the methods based on metamaterials are relatively inexpensive and could be developed and widely used in the image processing field.

Data availability statement

The original contributions presented in the study are included in the article/Supplementary Material; further inquiries can be directed to the corresponding authors.

Author contributions

YJ proposed the idea. YJ wrote the original manuscript. YJ and HH performed the simulation work. XM helped in revising the original manuscript, and XL supervised the research work.

Funding

This work was supported by the Key Scientific Research Projects of Institutions of Higher Learning of Henan Province Education Department (No. 21zx002) and the National Natural Science Foundation of China (No. 11974102).

Conflict of interest

The authors declare that the research was conducted in the absence of any commercial or financial relationships that could be construed as a potential conflict of interest.

Publisher's note

All claims expressed in this article are solely those of the authors and do not necessarily represent those of their affiliated organizations, or those of the publisher, the editors, and the reviewers. Any product that may be evaluated in this article, or claim that may be made by its manufacturer, is not guaranteed or endorsed by the publisher.

References

1. Pors A, Nielsen MG, Bozhevolnyi SI. Analog computing using reflective plasmonic metasurfaces. *Nano Lett* (2015) 15(1):791–7. doi:10.1021/nl5047297

2. Moeini MM, Sounas DL. Discrete space optical signal processing. *Optica.* (2020) 7(10):1325. doi:10.1364/OPTICA.400365

3. Kwon H, Sounas D, Cordaro A, Polman A, Alù A. Nonlocal metasurfaces for optical signal processing. *Phys Rev Lett* (2018) 121(17):173004. doi:10.1103/PhysRevLett.121.173004

4. Wesemann L, Panchenko E, Singh K, Della Gaspera E, Gómez DE, Davis TJ, et al. Selective near-perfect absorbing mirror as a spatial frequency filter for optical image processing. *APL Photon* (2019) 4(10):100801. doi:10.1063/1.5113650

5. Zangeneh-Nejad F, Fleury R. Topological analog signal processing. *Nat Commun* (2019) 10(1):2058. doi:10.1038/s41467-019-10086-3

6. Momeni A, Rajabalipanah H, Abdolali A, Achouri K. Generalized optical signal processing based on multioperator metasurfaces synthesized by susceptibility tensors. *Phys Rev Appl* (2019) 11(6):064042. doi:10.1103/PhysRevApplied.11.064042

7. Xu DY, He SS, Zhou JX, Chen SZ, Wen SC, Luo HL, et al. Goos–Hänchen effect enabled optical differential operation and image edge detection. *Appl Phys Lett* (2020) 116(21):211103. doi:10.1063/5.0006483

8. Wan L, Pan DP, Yang SF, Zhang W, Potapov AA, Wu X, et al. Optical analog computing of spatial differentiation and edge detection with dielectric metasurfaces. *Opt Lett* (2020) 45(7):2070. doi:10.1364/OL.386986

9. Huo PC, Zhang C, Zhu WQ, Liu MZ, Zhang S, Zhang S, et al. Photonic spin-multiplexing metasurface for switchable spiral phase contrast imaging. *Nano Lett* (2020) 20(4):2791–8. doi:10.1021/acs.nanolett.0c00471

10. Dobson KK, Jia W, Poon TC. Anisotropic edge enhancement in optical scanning holography with spiral phase filtering[J]. *Chin Opt Lett* (2016) 14(1):010006. doi:10.3788/COL201614.010006

11. Li ZH, Yu ZP, Hui H, Li HH, Zhong TT, Liu HL, et al. Edge enhancement through scattering media enabled by optical wavefront shaping. *Photon Res* (2020) 8(6):954. doi:10.1364/PRJ.388062

12. Luo HL, Ling XH, Zhou XX, Luo HL, et al.Hunan Provincial Key Laboratory of Intelligent Information Processing and Applications, College of Physics and Electronic Engineering, Hengyang Normal University, Hengyang 421002, China; School of Physics and Electronics, Hunan Normal University, Changsha 410081, China Spin-orbit interaction of a light beam under normal incidence at a sharp interface and its enhancement. *Acta Phys Sin* (2020) 69(3):034202. doi:10.7498/aps.69.20191218

13. Zhu TF, Zhou YH, Lou YJ, Ye H, Qiu M, Ruan ZC, et al. Plasmonic computing of spatial differentiation. *Nat Commun* (2017) 8(1):15391. doi:10.1038/ncomms15391

14. Goodman J. Introduction to fourier optics, second edition. *Opt Eng* (1996) 35(5):1513. doi:10.1117/1.6011212nd ed.

15. Qiu XD, Li FS, Zhang WH, Zhu ZH, Chen LX. Spiral phase contrast imaging in nonlinear optics: Seeing phase objects using invisible illumination. *Optica.* (2018) 5(2):208. doi:10.1364/OPTICA.5.000208

16. Kildishev AV, Boltasseva A, Shalaev VM. Planar photonics with metasurfaces. *Science* (2013) 339(6125):1232009. doi:10.1126/science.1232009

17. Genevet P, Capasso F, Aieta F, Khorasaninejad M, Devlin R. Recent advances in planar optics: From plasmonic to dielectric metasurfaces. *Optica.* (2017) 4(1):139. doi:10.1364/OPTICA.4.000139

18. Zhu TF, Lou YJ, Zhou YH, Zhang JH, Huang JY, Li Y, et al. Generalized spatial differentiation from the spin Hall effect of light and its application in image

processing of edge detection. *Phys Rev Appl* (2019) 11(3):034043. doi:10.1103/PhysRevApplied.11.034043

19. Long WJ, Pan JT, Guo XY, Liu XH, Lin HL, Zheng HD, et al. Optimized weak measurement of orbital angular momentum-induced beam shifts in optical reflection. *Photon Res* (2019) 7(11):1273. doi:10.1364/PRJ.7.001273

20. Onoda M, Murakami S, Nagaosa N. Hall effect of light. *Phys Rev Lett* (2004) 93(8):083901. doi:10.1103/PhysRevLett.93.083901

21. Bliokh KY, Bliokh YP. Conservation of angular momentum, transverse shift, and spin Hall effect in reflection and refraction of an electromagnetic wave packet. *Phys Rev Lett* (2006) 96(7):073903. doi:10.1103/PhysRevLett.96.073903

22. Bliokh KY, Bliokh YP. Polarization, transverse shifts, and angular momentum conservation laws in partial reflection and refraction of an electromagnetic wave packet. *Phys Rev E* (2007) 75(6):066609. doi:10.1103/PhysRevE.75.066609

23. Hosten O, Kwiat P. Observation of the spin Hall effect of light via weak measurements. *Science* (2008) 319(5864):787–90. doi:10.1126/science.1152697

24. Aiello A, Woerdman JP. Role of beam propagation in goos–hänchen and imbert–fedorov shifts. *Opt Lett* (2008) 33(13):1437. doi:10.1364/OL.33.001437

25. Thakur A, Berakdar J. Reflection and transmission of twisted light at phase conjugating interfaces. *Opt Express* (2012) 20(2):1301. doi:10.1364/oe.20.001301

26. Bliokh KY, Shadrivov IV, Kivshar YS. Goos–Hänchen and Imbert–Fedorov shifts of polarized vortex beams. *Opt Lett* (2009) 34(3):389. doi:10.1364/OL.34.000389

27. Merano M, Hermosa N, Woerdman JP, Aiello A. How orbital angular momentum affects beam shifts in optical reflection. *Phys Rev A* (2010) 82(2): 023817. doi:10.1103/PHYSREVA.82.023817

28. Bliokh KY, Aiello A. Goos–hänchen and imbert–fedorov beam shifts: An overview. *J Opt* (2013) 15(1):014001. doi:10.1088/2040-8978/15/1/014001

29. Xu DY, He SS, Zhou JX, Chen SZ, Wen SC, Luo HL, et al. Optical analog computing of two-dimensional spatial differentiation based on the Brewster effect. *Opt Lett* (2020) 45(24):6867. doi:10.1364/OL.413104

30. Bliokh KY, Samlan CT, Prajapati C, Puentes G, Viswanathan NK, Nori F, et al. Spin-Hall effect and circular birefringence of a uniaxial crystal plate. *Optica* (2016) 3(10):1039. doi:10.1364/OPTICA.3.001039

31. Fadeyeva TA, Volyar AV. Extreme spin-orbit coupling in crystal-traveling paraxial beams. *J Opt Soc Am A* (2010) 27(3):381. doi:10.1364/JOSAA.27.000381

32. Ciattoni A, Crosignani B, Di Porto P. Vectorial theory of propagation in uniaxially anisotropic media. *J Opt Soc Am A* (2001) 18(7):1656. doi:10.1364/JOSAA.18.001656

33. Ciattoni A, Palma C. Optical propagation in uniaxial crystals orthogonal to the optical axis: Paraxial theory and beyond. *J Opt Soc Am A* (2003) 20(11):2163. doi:10.1364/JOSAA.20.002163

34. Ciattoni A, Cincotti G, Palma C, Weber H. Energy exchange between the Cartesian components of a paraxial beam in a uniaxial crystal. *J Opt Soc Am A* (2002) 19(9):1894. doi:10.1364/JOSAA.19.001894

35. Ciattoni A, Palma C. Anisotropic beam spreading in uniaxial crystals. *Opt Commun* (2004) 231(1-6):79–92. doi:10.1016/j.optcom.2003.12.025

36. Cincotti G, Ciattoni A, Palma C. Laguerre–gauss and bessel–gauss beams in uniaxial crystals. *J Opt Soc Am A* (2002) 19(8):1680. doi:10.1364/JOSAA.19.001680

37. Zhang JB, Zhou KZ, Liang JH, Lai ZY, Yang XL, Deng DM, et al. Nonparaxial propagation of the Chirped Airy vortex beams in uniaxial crystal orthogonasl to the optical axis. *Opt Express* (2018) 26(2):1290. doi:10.1364/OE.26.001290

38. Li DD, Peng X, Peng YL, Zhang LP, Deng DM. Nonparaxial evolution of the Airy–Gaussian vortex beam in uniaxial crystal. *J Opt Soc Am B* (2017) 34(4):891. doi:10.1364/JOSAB.34.000891

39. Sun C, Lv X, Deng DM, Ma BB, Liu HZ, Hong WY, et al. Nonparaxial propagation of the radially polarized Airy-Gaussian beams with different initial launch angles in uniaxial crystals. *Opt Commun* (2019) 445:147–54. doi:10.1016/j.optcom.2019.04.021

40. Zhu WG, Zhuo LQ, Jiang MJ, Guan HY, Yu JH, Lu HH, et al. Controllable symmetric and asymmetric spin splitting of Laguerre–Gaussian beams assisted by surface plasmon resonance. *Opt Lett* (2017) 42(23):4869. doi:10.1364/OL.42.004869

41. Li L, Zhou ZY, Min CJ, Yuan XC. Extraordinary spin-orbit interaction in the plasmonic lens with negative index material[J]. *Opt Express* (2020) 28(18):26543. doi:10.1364/OE.401720